Ceramics International xxx (xxxx) xxx

Contents lists available at ScienceDirect

Ceramics International

journal homepage: www.elsevier.com/locate/ceramint

Reduced graphene oxide-CdSe nanorods: A synergistic platform for energy-efficient antibiotic removal under visible light

Subrata Mondal [a], Suvendu Ghosh [a], Tanusri Pal [b], Surajit Ghosh [a,*]

[a] Optoelectronic Materials Lab, Department of Physics, Vidyasagar University, Midnapore, 721102, India
[b] Department of Physics, Midnapore College (Autonomous), Midnapore, 721101, India

ARTICLE INFO

Handling Editor: P. Vincenzini

Keywords:
RGO-CdSe composite
Visible-light photocatalysis
Norfloxacin degradation
Apparent quantum yield
Energy-efficient photocatalyst

ABSTRACT

Developing visible-light-active nanocomposites for the energy-efficient removal of pharmaceutical contaminants is of growing environmental significance. In this work, a solution-processable reduced graphene oxide - CdSe (RGO-CdSe) nanorod composite was synthesized via a facile one-pot solvothermal route and evaluated as a robust photocatalyst for norfloxacin degradation under visible light. Structural and spectroscopic analyses confirm the formation of highly crystalline CdSe nanorods intimately coupled with two-dimensional RGO sheets, enabling enhanced light absorption and efficient interfacial charge transfer while preserving the CdSe crystal framework. The optimized RGO-CdSe composite achieves 80.4% norfloxacin degradation within 40 min, exhibiting pseudo-first-order kinetics with a rate constant of 0.057 min^{-1}, nearly four times higher than controlled-CdSe. Importantly, the composite demonstrates a 2.35-fold increase in apparent quantum yield (0.054%) and a 3.92-fold reduction in electrical energy per order (16.9 kWh m^{-3}), highlighting its superior energy efficiency. Radical scavenging studies identify photogenerated holes as the primary oxidative species, supported by hydroxyl and superoxide radicals. The photocatalyst retains approximately 90% of its activity after five successive cycles, with no detectable loss of crystallinity, confirming excellent structural and functional stability. These findings highlight RGO–CdSe nanocomposite as a promising platform for sustainable, energy-efficient, solar-driven remediation of antibiotic pollutants in water.

1. Introduction

The rapid and uncontrolled consumption of antibiotics has resulted in their persistent discharge into aquatic environments, posing serious ecological and public health concerns [1,2]. Antibiotic residues are frequently detected in wastewater and natural water bodies due to their incomplete metabolism and resistance to conventional biological treatment processes [3]. Their long-term accumulation contributes to the development of antimicrobial resistance and disrupts aquatic ecosystems [1,4]. Therefore, the development of efficient and sustainable strategies for the removal of antibiotic contaminants from water systems remains an urgent global priority.

Among various advanced treatment technologies, semiconductor-based photocatalysis has emerged as a promising approach owing to its ability to utilize solar energy for the degradation of recalcitrant organic pollutants [5–7]. Visible-light-driven photocatalysis is particularly attractive, as visible light constitutes the major fraction of the solar spectrum. However, the practical efficiency of many semiconductor photocatalysts is often limited by rapid recombination of photogenerated electron-hole pairs and insufficient interfacial charge transport, which significantly reduces quantum efficiency [8,9].

To address these challenges, rational heterostructure engineering and composite design strategies have been widely explored to enhance charge separation, extend light absorption, and accelerate surface redox reactions [10–12]. Constructing intimate interfacial contact between semiconductors and conductive carbonaceous materials has proven particularly effective in facilitating directional electron transport and suppressing recombination losses [13,14].

Reduced graphene oxide (RGO) has emerged as an excellent conductive scaffold for photocatalytic applications due to its high electrical conductivity, large specific surface area, tunable surface functionalities, and strong electron-accepting capability [15,16]. RGO has been extensively incorporated with semiconductors to enhance visible-light photocatalytic degradation of organic pollutants, where it facilitates rapid interfacial electron transfer and provides a conductive pathway for charge carrier migration, thereby suppressing electron-hole

* Corresponding author.
E-mail address: surajit@mail.vidyasagar.ac.in (S. Ghosh).

https://doi.org/10.1016/j.ceramint.2026.03.412
Received 30 January 2026; Received in revised form 12 March 2026; Accepted 27 March 2026
Available online 28 March 2026

recombination and enhancing apparent quantum efficiency [17–19]. Several RGO-based composite systems have demonstrated significantly enhanced degradation kinetics toward antibiotic and dye contaminants compared to their pristine semiconductor counterparts, highlighting its critical role in interfacial charge modulation [17–19].

On the other hand, CdSe is a narrow bandgap chalcogenide semiconductor with strong visible-light absorption characteristics [20,21]. In particular, CdSe nanorods possess anisotropic one-dimensional morphology that promotes directional charge transport along the longitudinal axis, thereby facilitating spatial separation of photogenerated carriers. Their high aspect ratio and tunable electronic structure make them attractive candidates for photocatalytic and photoelectrochemical applications under visible irradiation.

RGO-CdSe composites have been investigated for diverse applications, such as LDL detection [22], enhanced desulfurization [23], optoelectronic property modulation [24], photoelectrochemical hydrogen production [25], dye degradation [26], and electrochemical sensing [27]; however, their systematic exploration as visible-light-driven photocatalysts for antibiotic remediation, particularly with detailed correlation between interfacial charge transfer and quantum efficiency, remains limited.

In this context, the present work reports the facile synthesis of an RGO-CdSe nanorod composite via a one-step solvothermal approach and evaluates its photocatalytic performance toward antibiotic degradation under visible light. Comprehensive structural, optical, and electrochemical characterizations are carried out to elucidate the interfacial charge transport mechanism and establish its direct correlation with photocatalytic efficiency, apparent quantum yield, and energy consumption parameters. This study establishes RGO-CdSe nanorods as a promising hybrid semiconductor nanocomposite platform for sustainable, energy-efficient remediation of antibiotic contaminants in water.

2. Experimental section

2.1. Chemicals

Reagents of analytical quality were utilized as obtained, with no subsequent purification. Potassium persulfate ($K_2S_2O_8$), graphite powder, sodium nitrate ($NaNO_3$), phosphorus pentoxide (P_2O_5), cadmium nitrate tetrahydrate [$Cd(NO_3)_2{\cdot}4H_2O$], sodium selenite (Na_2SeO_3), and the antibiotic norfloxacin were obtained from Sigma-Aldrich. Chemicals including ethanol, potassium permanganate ($KMnO_4$), hydrogen peroxide (H_2O_2), hydrochloric acid (HCl), sulfuric acid (H_2SO_4), ethylenediamine (ED), 2-propanol (IPA), and ethylenediaminetetraacetic acid disodium (EDTA–Na_2) were sourced from Merck.

2.2. Material preparation

An one-step solvothermal strategy was employed to synthesize solution-processable RGO-CdSe photocatalysts, renowned for its simplicity, cost-effectiveness, and single-pot nanomaterial synthesis capability. Pre-treated graphite oxide was thoroughly exfoliated into graphene oxide (GO) [28]. Subsequently, varying amounts of GO (20, 30, 40, 50, and 60 mg) were uniformly dispersed in ethylenediamine (ED)-double-distilled water (DDW) mixed solvent (volume ratio 2:1) and sonicated for 10 min in five individual beakers. 2 mmol each of Cd $(NO_3)_2{\cdot}4H_2O$ and Na_2SeO_3 were added to the five beakers, followed by vigorous stirring for 30 min to ensure homogeneous mixing. The resulting mixtures were sealed in five individual Teflon-lined autoclaves and heated at 170 °C for 12 h under autogenous pressure. After natural cooling, the products were centrifuged and repeatedly washed with DDW to remove unreacted species and residual metal ions, then vacuum-dried to obtain five refined RGO-CdSe nanocomposite powders, designated as 20RGO-CdSe, 30RGO-CdSe, 40RGO-CdSe, 50RGO-CdSe, and 60RGO-CdSe. For comparison, pristine CdSe nanorods (controlled-CdSe) were synthesized under identical conditions without GO. Unless otherwise specified, RGO-CdSe refers to the 40RGO-CdSe sample. A schematic representation of the stepwise formation process of the RGO-CdSe composite is shown in Fig. 1.

2.3. Materials characterization

X-ray diffraction (XRD) patterns of both CdSe and RGO-CdSe samples were collected in the 2θ range of 5° to 60° using a Rigaku Miniflex II diffractometer equipped with Cu K_α radiation (λ = 0.15418 nm), operated at 30 kV and 10 mA. The morphological features of the materials were examined through field emission scanning electron microscopy (FESEM; Zeiss, Gemini-II Cryo). Transmission electron microscopy (TEM) and high-resolution TEM (HRTEM) imaging were employed to analyze the crystallinity and nanoscale architecture of the RGO-CdSe system, using a JEOL F200 instrument at 200 kV accelerating voltage. The measurements of specific surface area and porosity for controlled-CdSe and RGO-CdSe composite were conducted using nitrogen adsorption–desorption data obtained from a Quantachrome Autosorb iQ-MPx analyzer. Raman spectroscopy was conducted using a Horiba Scientific labRAM HR micro-Raman spectrometer. Optical absorption in the UV–visible domain and photoluminescence (PL) emission spectra of both controlled-CdSe and RGO-CdSe composites were measured with an Agilent Cary series UV-vis-NIR spectrophotometer and a Hitachi F-7000 fluorescence spectrophotometer, respectively.

2.4. Measurement of photocatalytic activity

To assess the visible-light photocatalytic performance, degradation of norfloxacin was studied in the presence of the synthesized photocatalysts. A suspension was prepared by dispersing 18 mg of photocatalyst in 40 mL of a 12.5 mg/L aqueous norfloxacin solution. The reaction took place in a quartz vessel illuminated with 1000 W tungsten halogen lamp at room temperature. A tungsten-halogen lamp was selected as the visible-light source due to its cost-effectiveness, high stability, and adequate spectral match in the visible range when filtered, enabling reproducible lab-scale tests without the need for expensive solar simulators. Prior to illumination, the mixture was magnetically agitated in the dark for 30 min to reach adsorption–desorption equilibrium. During the degradation test, 4 mL solution were taken every 5 min and analyzed using UV–vis spectroscopy to monitor changes in norfloxacin concentration. The efficiency of photocatalytic degradation was determined from the concentration ratio C/C_0, where C_0 corresponds to the initial concentration of the pollutant, and C refers to its concentration after an irradiation period of duration t.

3. Results and discussion

3.1. Materials characterization

The powder X-ray diffraction (XRD) technique was adopted to examine the phase structure and crystallinity of the as-prepared controlled-CdSe and RGO-CdSe nanocomposites, and the corresponding XRD patterns are displayed in Fig. 2A. The characteristic peaks observed for controlled-CdSe can be indexed to the (100), (002), (101), (102), (110), (103), and (112) planes, which are consistent with the hexagonal wurtzite structure of CdSe, as referenced by the JCPDS card no. 08-0459 [29]. Although, the XRD pattern is dominated by hexagonal characteristics, certain regions show potential cubic phase contributions. These potential cubic contributions are minor and cannot be definitively confirmed without advanced analytical techniques such as Rietveld refinement. Upon incorporation of RGO, the XRD spectrum for RGO-CdSe composite retains all the characteristic peaks of CdSe without any noticeable shift or broadening. Furthermore, the intense and well-resolved diffraction peak at 2θ = 25.5° points to a long-range crystalline order along the c-axis of the hexagonal phase. The result implies that the CdSe lattice structure remains essentially unchanged in

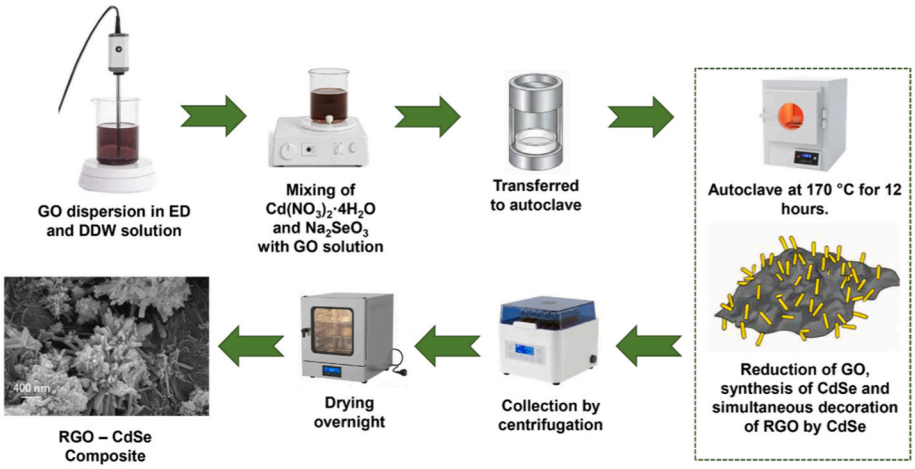

Fig. 1. Schematic depiction of the synthesis route for the RGO–CdSe composite.

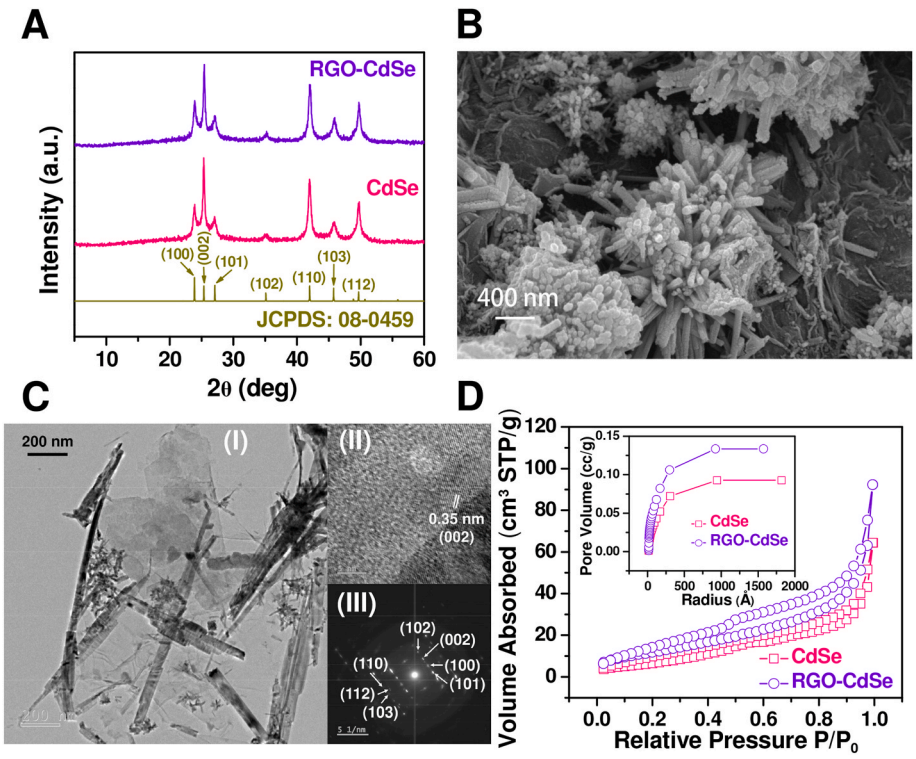

Fig. 2. Structural and morphological characterization of RGO–CdSe: **(A)** X-ray diffraction patterns, **(B)** SEM and **(C)** (I) TEM images of the composite, (II) HRTEM image and (III) SAED pattern of CdSe on RGO sheets. **(D)** Nitrogen adsorption–desorption isotherms; inset: pore-volume distribution.

the presence of RGO. Moreover, no additional peaks corresponding to oxygen-containing functional groups (typically observed near ~10.4° for GO) are present [30], confirming the effective chemical reduction of GO to RGO during the synthesis. The absence of a broad RGO peak near ~26° may be attributed to the overlap with the (002) peak of CdSe or the low scattering intensity of the few-layered RGO sheets. Overall, the XRD results demonstrate the preservation of the crystalline wurtzite CdSe phase in the composite and the successful formation of the RGO-CdSe composite structure. The other four RGO-CdSe composites with varying RGO content exhibit similar XRD patterns to that of the standard RGO-CdSe composite. Fig. S1A in the Supporting Information (SI) presents the XRD profiles of all composites.

The surface morphology and structural integration of the controlled-CdSe and the RGO-CdSe composite materials were systematically investigated using SEM, as depicted in Fig. S1B in the SI, and Fig. 2B, respectively. The formation of nanorod morphology is clearly observed in the SEM image of controlled-CdSe. Whereas, the micrographs of RGO-CdSe composite clearly reveal that the CdSe nanorods are attached onto the surface of RGO sheets, suggests interfacial coupling between CdSe and RGO. Such intimate contact is expected to promote rapid charge migration across the junction, a key factor in improving photocatalytic activity. The EDX profile of the RGO-CdSe composite exhibits pronounced peaks of Cd and Se, verifying the presence of CdSe. In addition, characteristic signals of carbon and oxygen, arising from the RGO support, are also observed in the spectrum (Fig. S1C, in SI). These findings unambiguously confirm the successful integration of CdSe nanostructures onto the RGO scaffold.

Detailed insights into the microstructure of the RGO-CdSe composite were acquired through TEM and high-resolution TEM (HRTEM) analyses, as illustrated in Fig. 2C(I). The TEM images reveal the distribution

of CdSe nanorods well-adhered to the wrinkled, two-dimensional surface of the RGO sheets. This spatially extended and well-integrated assembly suggests a robust interfacial interaction between the semiconductor and the carbonaceous support. Such intimate contact is expected to promote efficient charge carrier separation and transfer at the CdSe–RGO junction, which is crucial for potential photocatalytic applications. High-resolution TEM [Fig. 2C(II)] reveals well-resolved lattice fringes with interplanar spacings of approximately 0.35 nm, corresponding to the (002) plane. These values are in close agreement with the d-spacings obtained from XRD analysis, thereby confirming the crystallographic identity of the CdSe phase. Notably, the HRTEM images do not exhibit any characteristic features indicative of a core–shell architecture. However, regions of uneven contrast in the micrographs can be attributed to localized stacking or folding of multiple RGO layers, resulting in areas of increased electron density [31]. To further clarify the crystallographic structure of the CdSe nanorods, selected area electron diffraction (SAED) analysis was performed. The SAED pattern [Fig. 2C(III)] reveals sharp and well-resolved diffraction spots with clear reciprocal-lattice symmetry, which can be indexed to the (100), (002), (101), (102), (110), (103), and (112) planes of CdSe. These observations are fully consistent with the XRD results and highlight the structurally robust nature of the CdSe nanorods, which is favorable for efficient charge transport and visible-light-driven photocatalytic degradation of norfloxacin.

Nitrogen adsorption–desorption measurements were carried out to systematically assess the surface area and pore structure of controlled-CdSe and the RGO-CdSe composite, and the results were analyzed using Brunauer–Emmett–Teller (BET) theory. The surface area measurements were carried out using the multipoint BET approach, applying the standard BET linear equation [32,33]:

$$\frac{P/P_0}{W\left(1-P/P_0\right)}=\frac{1}{W_mC}+\frac{C-1}{W_mC}\left(P/P_0\right)$$

where P/P_0 represents the relative pressure, W denotes the volume of nitrogen gas adsorbed at equilibrium, and W_m corresponds to the monolayer adsorption capacity. The parameter C is a dimensionless BET constant that reflects the energetic affinity between the adsorbate molecules and the solid surface in the first adsorption layer, it increases exponentially with the magnitude of the heat of adsorption. A linear BET plot was constructed by plotting $\frac{1}{W\left(1-P/P_0\right)}$ vs. P/P_0, and the linearity of this plot indicates good conformity of the experimental data with the BET theoretical model. The isotherms, presented in Fig. 2D, displayed Type IV characteristics according to the IUPAC classification, with a well-defined H1-type hysteresis loop, signifying capillary condensation within mesopores [34]. Such features are characteristic of mesoporous solids.

The BET analysis revealed that the RGO-CdSe composite exhibits a significantly larger surface area (45.5 $m^2\ g^{-1}$) than controlled-CdSe (29.0 $m^2\ g^{-1}$). The higher surface area in the composite is expected to enhance photocatalytic performance by providing an increased density of accessible reaction sites [35]. Moreover, the pore volume of RGO-CdSe (0.134 $cm^3\ g^{-1}$) was found to be greater than that of CdSe (0.09 $cm^3\ g^{-1}$), which likely facilitates improved adsorption and molecular diffusion of reactants. The pore volume distribution with pore radius is presented in the inset of Fig. 2D. The Barrett–Joyner–Halenda (BJH) pore-size distribution further confirms the coexistence of mesopores and macropores within the RGO-CdSe structure, which is advantageous for mass transport during catalytic processes.

To complement the surface textural findings, Raman spectroscopy was employed to investigate the structural and interfacial characteristics of the RGO-CdSe composite. Fig. 3A displays the Raman spectra of the synthesized RGO-CdSe composite, providing insights into its structural characteristics and associated modifications. Two pronounced peaks are observed at approximately 1340 cm^{-1} and 1592 cm^{-1}, corresponding to the D and G bands, respectively. The D band arises from lattice imperfections or disorder, associated with the breathing vibration of the K-point phonon having A_{1g} symmetry among carbon atoms. In contrast, the G band originates from the in-plane stretching vibrations of E_{2g} phonons within sp^2-hybridized carbon networks [36]. In addition to these characteristic features of RGO, several additional peaks appear at lower wavenumbers, attributable to the CdSe component. The prominent band at 206 cm^{-1} corresponds to the first-order longitudinal optical (1LO) phonon vibration, while the peaks observed at 287 cm^{-1} and 405 cm^{-1} are assigned to surface phonon contributions and the second-order longitudinal optical (2LO) phonon, respectively [36].

The relative intensity ratio of the D and G bands (I_D/I_G) serves as an indicator of the degree of graphitization, which significantly influences the dielectric behavior of carbonaceous materials. For the RGO-CdSe composite, the I_D/I_G value is determined to be approximately 1.28, signifying substantial reduction of graphene oxide and confirming the successful formation of reduced graphene oxide within the hybrid structure.

In catalytic systems, particularly in photocatalysis and adsorption-mediated pollutant removal, the availability of surface-active sites plays a crucial role in dictating performance. The extended surface area of RGO-CdSe provides a larger interface for the adsorption of pollutant molecules and enhances contact between reactants and catalytic centers. Therefore, whether through direct adsorption or photo-induced degradation mechanisms, materials possessing greater specific surface areas are inherently more efficient, making RGO-CdSe a superior candidate for environmental remediation applications.

The effectiveness of a photocatalyst largely depends on its ability to harvest light across a broad spectral range for exciton generation, together with efficient photoinduced charge separation that minimizes electron–hole recombination. To evaluate both the optical absorption and charge transfer characteristics, UV–Vis and photoluminescence (PL) spectroscopic analyses were performed, as shown in Fig. 3B and C, respectively. The absorption profile of CdSe exhibits a distinct peak around 620 nm (Fig. 3B). In contrast, the RGO-CdSe composite displays markedly enhanced absorption throughout the visible region (200–800

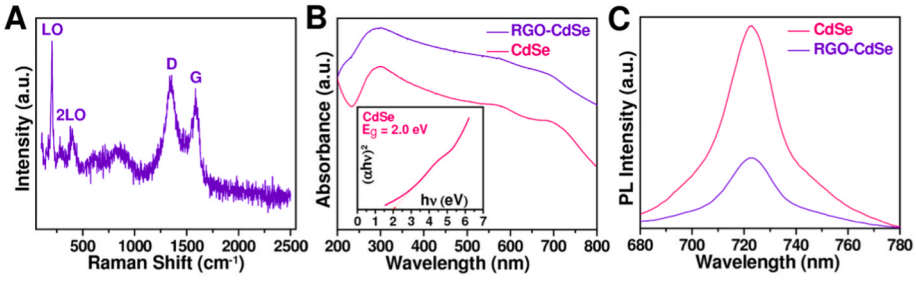

Fig. 3. Optical properties of the RGO–CdSe composite: **(A)** Raman spectra, **(B)** UV–vis absorption spectra with the inset showing the Tauc plot $[(\alpha h\upsilon)^2$ vs photon energy] for CdSe, and **(C)** photoluminescence spectra demonstrating emission quenching in the composite, indicative of efficient photoinduced charge transfer.

nm). The composite shows improved visible-light absorption relative to the pristine semiconductor, which contributes to enhanced photocatalytic performance under solar irradiation [37]. The optical band gap (E_g) of CdSe was derived from Tauc's relation, $\alpha h\nu = A(h\nu - E_g)^n$, where $n = 1/2$ for a direct transition and $n = 2$ for an indirect transition [38,39]. The variation of $(\alpha h\nu)^2$ with photon energy ($h\nu$), presented in the inset of Fig. 3B, yielded a band gap of approximately 2.00 eV. Compared to bulk CdSe ($E_g \approx 1.74\ eV$) [40], this represents a blue shift, which can be attributed to the quantum confinement effect in CdSe nanorods.

The photoluminescence (PL) spectrum of the controlled-CdSe is displayed in Fig. 3C. Under 610 nm excitation, the CdSe nanorods exhibit a distinct photoluminescence peak at 723 nm. The red-shifted emission relative to their optical bandgap (~2.0 eV) confirms a measurable Stokes shift. This shift arises from carrier relaxation into lower-energy states before radiative recombination, and is further influenced by defect-related trap states at the nanorod surface. The PL characteristics therefore indicate contributions from both intrinsic band-edge transitions and defect-assisted recombination pathways. However, this emission is drastically suppressed in the RGO-CdSe nano composite, indicating a strong interfacial interaction between CdSe and RGO. The quenching of PL intensity arises from efficient charge separation facilitated by the RGO sheets, which serve as electron acceptors and suppress radiative recombination pathways. Similar PL suppression behavior due to interfacial electron transfer in RGO/semiconductor Schottky heterojunction systems and semiconductor-based heterojunction systems has been widely reported in recent studies [41,42]. When exposed to visible light, electrons in CdSe transition from the valence band (VB) to the conduction band (CB), leaving photoinduced holes in the VB. The excited electrons are rapidly transferred to the RGO matrix due to its high conductivity and large surface area, thereby preventing recombination with the photo-generated holes. Simultaneously, the holes remaining in the VB of CdSe actively participate in oxidation reactions, contributing synergistically to the photocatalytic process. In the context of wastewater treatment, this enhanced charge carrier separation significantly boosts the generation of reactive oxygen species (ROS), including hydroxyl radicals ($OH^{\cdot}$) and superoxide anions ($O_2^{-\cdot}$), through both oxidative and reductive pathways. These ROS are highly effective in decomposing persistent organic pollutants like norfloxacin, a widely used fluoroquinolone antibiotic known for its environmental persistence and resistance to conventional treatment methods.

3.2. Visible-light-induced photocatalytic degradation of norfloxacin by RGO-CdSe composite

Initially, the self-degradation of norfloxacin under identical experimental conditions was investigated using optical absorption measurements. An aqueous solution of norfloxacin was exposed to light for 40 min, and its absorption spectra were recorded before and after illumination. As shown in Fig. S2A in the SI, no significant change was observed in the absorption spectra over the experimental time frame. This indicates that norfloxacin does not undergo noticeable self-photolysis under the applied illumination conditions. To assess the role of adsorption in the degradation process, experiments were conducted in the dark using RGO-CdSe composites containing different amounts of RGO. The adsorption spectrum of RGO-CdSe for different time is displayed in Fig. S2B, in SI. After this initial phase, no further significant changes were observed, indicating that adsorption–desorption equilibrium was achieved within 30 min (Fig. S2B, in SI). The adsorption of all the RGO-CdSe composite with the varying RGO content was also studied. Within the first 30 min, norfloxacin removal ranged between 37% and 51%, depending on the RGO content in the composite (Fig. S2C in the SI).

Upon reaching equilibrium, light irradiation was applied to investigate the photocatalytic activity of both CdSe and the RGO-CdSe composite for the degradation of norfloxacin in aqueous solution at ambient condition. The progressive reduction of the characteristic absorption peak of norfloxacin with increasing illumination time, in the presence of controlled-CdSe and RGO-CdSe catalysts, is depicted in Fig. S3A and S3B, respectively, in the SI. A comparative analysis of the degradation curves of CdSe and the RGO-CdSe composite is provided in Fig. 4A. As shown in Fig. 4A, the controlled-CdSe exhibited relatively low photocatalytic degradation efficiency, achieving only 30.9% after 40 min of light irradiation. In contrast, the RGO-CdSe nanocomposites demonstrated significantly enhanced degradation performance by 80.4% in 40 min under identical experimental conditions, indicating that the incorporation of RGO nanosheets effectively improves the photocatalytic activity of CdSe.

To elucidate the underlying mechanism of photocatalytic degradation, a detailed kinetic investigation was performed. The photocatalytic reaction kinetics were interpreted using the widely accepted Langmuir - Hinshelwood (L-H) model, which is applicable under conditions where adsorption-desorption equilibria significantly influence reaction rates [43,44]. According to the Langmuir-Hinshelwood (L-H) kinetic model, the photocatalytic reaction rate (r) can be expressed as [45]:

$$r = -\frac{dC}{dt} = \frac{k_r K C}{1 + KC}$$

where C is the pollutant concentration in solution ($mg\,L^{-1}$), k_r is the intrinsic reaction rate constant ($mg\,L^{-1}\,min^{-1}$), and K is the adsorption equilibrium constant ($L\,mg^{-1}$). This formulation assumes adsorption - desorption equilibrium on the catalyst surface and that the reaction occurs exclusively at adsorbed sites.

At low pollutant concentrations ($KC \ll 1$), the denominator simplifies to unity ($1 + KC = 1$), yielding:

$$r = -\frac{dC}{dt} \approx k_r K C$$

Defining the apparent pseudo-first-order rate constant as $k = k_r K$, the rate law simplifies to:

$$r = -\frac{dC}{dt} = kC$$

which integrates to the familiar pseudo-first-order expression [46–48]:

$$ln(C_0 / C) = kt$$

where C_0 and C are the initial and instantaneous pollutant concentrations, respectively, and t is the irradiation time. As shown in Fig. 4B, the linearity of the $ln(C_0/C)$ versus t plot enabled the determination of k values through linear regression. The RGO-CdSe composite exhibited a rate constant of 0.057 min^{-1}, which is approximately 3.8 times greater than that observed for the controlled-CdSe (0.015 min^{-1}). The observed improvement in photocatalytic behavior is due to the inclusion of RGO, which not only facilitates efficient charge separation and transport by serving as a conductive electron acceptor but also increases the specific surface area of the composite, as confirmed by BET measurements. This increased surface area provides a greater number of accessible catalytic sites, enabling more effective interaction with norfloxacin molecules and thereby improving the overall photocatalytic performance.

The incident photon flux plays a pivotal role in governing the kinetics of photocatalytic processes, as it dictates the rate of photogeneration of charge carriers. A key parameter to quantify the photon to product conversion efficiency is the quantum yield (QY), defined as the ratio between the number of reactant molecules converted and the number of photons theoretically absorbed over a given time. This parameter offers critical insight into the efficiency with which absorbed photons are utilized to drive the target chemical transformation. However, precise determination of the QY requires knowledge of the action spectrum, that is, the wavelength resolved photocatalytic response within the spectral window relevant to the photocatalyst's absorption profile. Such spectral data are essential to establish the correlation

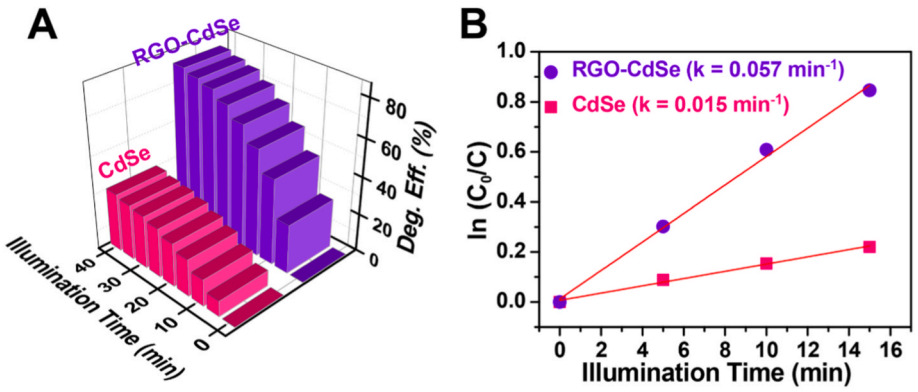

Fig. 4. Photocatalytic performance under visible-light illumination: **(A)** degradation efficiency over time and **(B)** first-order kinetics [$\ln(C_0/C)$ vs. time] for CdSe and RGO–CdSe.

between excitation energy and catalytic performance.

In real-world systems, especially in turbid or colloidal dispersions, quantifying the exact number of photons absorbed by the photocatalyst is complicated by light scattering, reflection, and nonuniform absorption. This limitation makes the accurate assessment of QY challenging under practical conditions. To address these complexities, the Apparent Quantum Yield (AQY) is widely used as an effective alternative. Unlike QY, AQY is calculated based on the number of incident photons without requiring the actual number of absorbed photons, thereby offering a reliable metric for evaluating photocatalytic performance under experimental illumination.

In this study, the AQY percentage was determined using the following relation [49,50]:

$$\text{Apparent Quantum Yield (AQY)} = = \frac{\textit{Number of degraded molecule}}{\textit{Number of incident photon}} \times 100\ \%$$

The number of incident photons was estimated from the total energy irradiated onto the photocatalytic suspension, divided by the energy of a single photon corresponding to the optical band gap of the active material. Notably, in our system, photoexcitation occurs within the CdSe component of the RGO-CdSe composite, leading to the generation of excitons that subsequently dissociate into free electrons and holes. These charge carriers are the primary contributors to the photocatalytic degradation of norfloxacin. Therefore, the band gap of CdSe was used to calculate the energy per photon, assuming that light absorption and exciton generation occur predominantly in CdSe. Furthermore, the experiments were conducted under broadband white light illumination. Only the spectral fraction matching the absorption band of CdSe is effectively absorbed by CdSe. This assumption inherently underestimates the true QY, as a significant portion of the incident light is also absorbed by RGO, while part of it is additionally lost due to scattering. Hence, the actual QY under ideal absorption conditions is expected to be significantly higher than the calculated AQY. After 40 min of visible light exposure, the RGO-CdSe nanocomposite demonstrated an AQY of 0.054%, which is approximately 2.35 times higher than that of controlled-CdSe (0.023%).

A tungsten halogen lamp powered the degradation of norfloxacin, with electrical energy as the key cost. The energy required to reduce pollutants was quantified, essential for the economic and sustainable viability of water treatment, particularly for large-scale or decentralized systems. To this end, a standard performance indicator known as Electrical Energy per Order (EE/O) was utilized. This parameter is defined as the amount of electrical energy (expressed in kilowatt-hours) required to decrease the concentration of a target pollutant by one logarithmic order (i.e., by 90 percent) in a unit volume of contaminated water, typically one cubic meter (1000 L). The EE/O value provides a practical measure of energy demand and process efficiency and is widely used in evaluating advanced oxidation processes. The mathematical expression for EE/O is given by Refs. [51–53]:

$$\frac{EE}{O} = \frac{P \times t \times 1000}{V \times log(C_0/C)}$$

where P corresponds to the power of the lamp (kW), t indicates the irradiation time (h), V is the volume of the solution (L), and $log(C_0/C)$ is the logarithmic reduction in pollutant concentration. The illumination dose $(in\ kWm^{-3})$ was calculated using the following relation [51–53]: Illumination dose $= P \times t \times 1000/V$. The dependence of $log(C_0/C)$ on the calculated illumination dose is graphically represented in Fig. S3D in SI, highlighting the degradation kinetics under different energy exposures. Using the above framework, the EE/O for the degradation of norfloxacin in the presence of controlled-CdSe photocatalyst was determined to be 66.2 kWh m^{-3} per order of magnitude reduction. In contrast, under identical photocatalytic conditions, including with initial norfloxacin concentration of 12.5 mg L^{-1} and a catalyst loading of 0.45 g L^{-1}, the RGO-CdSe nanocomposite exhibited a significantly lower EE/O value of 16.9 kWh m^{-3} per order. This reduction in energy consumption, by nearly 3.92-fold, highlights the superior efficiency of the RGO-CdSe composite system. The low EE/O value of the RGO-CdSe composite marks a significant step toward energy-efficient, cost-effective water purification. Reduced energy demand boosts economic viability and supports sustainable photocatalysis. This highlights the potential of optimized RGO-CdSe for scalable wastewater treatment and pharmaceutical residue removal.

A marked improvement in CdSe's photocatalytic performance was achieved through hybridization with RGO, forming RGO-CdSe nanocomposites with varying GO contents (20-60 mg). Norfloxacin degradation studies (Figs. 5A and S4A) revealed a non-monotonic trend, with efficiency peaking at 40 mg RGO. Kinetic analysis (Fig. 5B) confirmed the highest rate constant (k) for the 40RGO-CdSe composite, indicating optimal charge separation and light utilization. At low RGO levels, poor electron transfer limits performance, while excess RGO (>40 mg) shields CdSe and reduces active sites. AQY measurements (Fig. 5C) followed the same trend, validating the optimal composition. Energy efficiency analysis (EE/O, Fig. 5D) showed the lowest value for 40RGO-CdSe, demonstrating superior energy utilization. Overall, 40RGO-CdSe exhibited the highest degradation rate, maximum AQY, and lowest EE/O, making it the most effective and energy-efficient photocatalyst for norfloxacin degradation.

Additionally, we have investigated the degradation of another commonly used antibiotic, tetracycline, using the same RGO–CdSe composite under identical experimental conditions. Interestingly, a similar variation in photocatalytic efficiency and rate constant was observed, further confirming the reproducibility and reliability of the RGO–CdSe system for efficient antibiotic degradation under visible

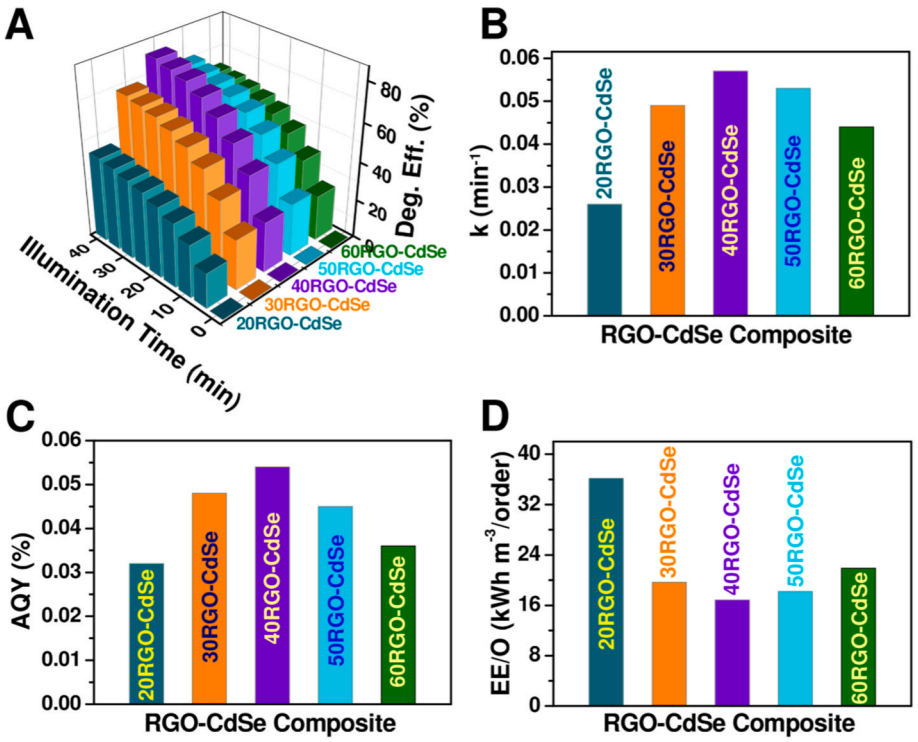

Fig. 5. Effect of RGO loading on photocatalytic activity: **(A)** degradation efficiency, **(B)** reaction rate, **(C)** apparent quantum yield (AQY), and **(D)** energy consumption per order (EE/O).

light.

Norfloxacin primarily degrades via oxidative pathways in water

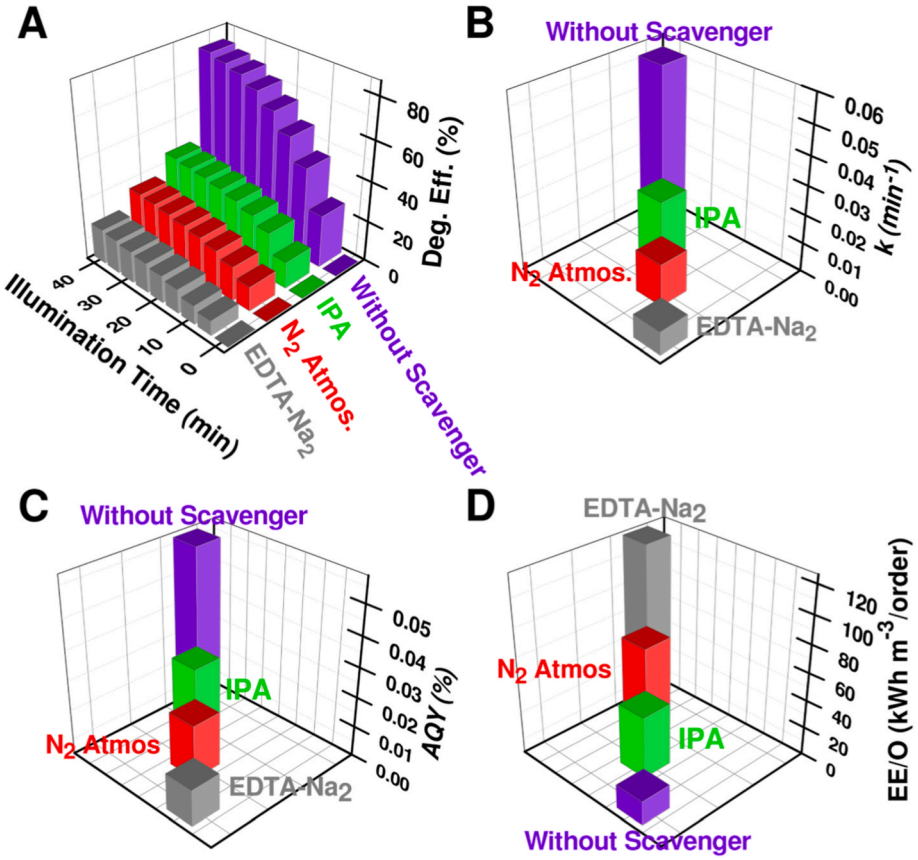

Fig. 6. Influence of radical scavengers on RGO–CdSe photocatalysis: **(A)** degradation efficiency, **(B)** kinetic constant, **(C)** AQY, and **(D)** EE/O with and without scavengers.

[54–57]. To elucidate the mechanism over RGO-CdSe, radical scavenging experiments were performed to identify the roles of specific reactive species. To this end, ethylenediaminetetraacetic acid disodium salt (EDTA-Na_2) was employed to quench photogenerated holes (h^+), 2-propanol (IPA) acted as a scavenger for hydroxyl radical ($OH^·$), and nitrogen purging was carried out to suppress superoxide radical ($O_2^{-·}$) generation by removing dissolved O_2 [58–61]. The temporal decline of normalized norfloxacin peaks in the presence of various scavengers is presented in Fig. S5A in SI. A comparative analysis of the degradation efficiencies is presented in Fig. 6A. The *k* values were extracted from the linear fitting of $ln(C_0/C)$ vs. *t* plots, enabling a quantitative evaluation of degradation kinetics under each scavenger condition and are presented in Fig. 6B. The presence of EDTA–Na_2 resulted in a significant suppression of photocatalytic activity, yielding only 19% degradation efficiency. This pronounced decrease highlights the predominant role of photogenerated holes in initiating the oxidative decomposition of norfloxacin. Conversely, the introduction of IPA and nitrogen gas led to moderate reductions in degradation efficiency, registering values of 47% and 60%, respectively. These results indicate that while $OH^·$ and $O_2^{-·}$ radicals also contribute to degradation. The EE/O values were extracted from the linear fitting of $ln(C_0/C)$ vs. *illumination dose* for different scavengers and are presented in Fig. S5B in SI. A comparative summary of the AQY and EE/O per order for each scavenger condition is provided in Fig. 6C and D, respectively.

The superior photocatalytic performance of the RGO–CdSe composite arises from a synergistic interplay between structural integration, optical enhancement, and electronic modulation. The intimate interfacial contact between CdSe nanorods and RGO sheets facilitates rapid electron extraction from the conduction band of CdSe to the conductive RGO network, thereby suppressing bulk and surface recombination, as evidenced by PL quenching. Simultaneously, the increased specific surface area enhances pollutant adsorption and interfacial reaction probability, while the high electrical conductivity of RGO promotes efficient charge transport. The optimized RGO loading (40 mg of GO) provides a balanced architecture, ensuring effective electron scavenging without excessive light shielding, leading to maximum AQY and minimum EE/O.

Based on these findings, a mechanistic pathway is proposed: under visible light illumination, CdSe nanorods generate excitons that subsequently separate into free electrons in the CB and holes in the VB of CdSe. The photogenerated electrons are rapidly transferred to the RGO sheets, which act as conductive channels and suppress recombination. The retained holes on CdSe subsequently oxidize norfloxacin molecules directly. Meanwhile, the migrated electrons reduce surface-adsorbed O_2 to form $O_2^{-·}$ radicals, and secondary reactions involving water or hydroxide ions produce $OH^·$ radicals. These ROS further oxidize norfloxacin through multiple routes, including defluorination, hydroxylation, and decarboxylation. The integration of RGO with CdSe not only suppresses charge carrier recombination but also prolongs the lifetimes of active species, thereby enhancing the generation of ROS and accelerating photocatalytic efficiency. Fig. 7 presents a schematic representation of the formation of reactive species and the proposed degradation mechanism of norfloxacin [62]. Although the proposed charge transfer mechanism is supported by experimental observations, further theoretical validation through density functional theory (DFT) calculations would provide deeper insight into band alignment and interfacial charge redistribution in the RGO-CdSe heterostructure.

Efficient recovery and reuse of photocatalysts with minimal loss of activity are crucial from both economic and environmental perspectives. Although separating solid catalysts from liquid media can sometimes be challenging, in this study, the RGO-CdSe composite was conveniently retrieved through simple centrifugation, followed by mild thermal treatment before reuse. Remarkably, the catalyst preserved about 90% of its degradation efficiency even after five successive photocatalytic cycles, as shown in Fig. S6A (Supporting Information). To evaluate whether repeated use affected the structural order and crystallinity of the RGO- CdSe photocatalyst, X-ray diffraction measurements were performed after the recycling tests. As presented in Fig. S6B, the diffraction features of the composite exhibited no discernible change after five cycles, confirming the excellent structural integrity and phase stability of the RGO-CdSe material during repeated photocatalytic operations. A comparative analysis with previously reported photocatalysts for antibiotic degradation is presented in Table T1, in SI, demonstrating the competitive performance of the optimized RGO-CdSe composite.

4. Conclusion

In summary, this study demonstrates the successful development of a solution-processable RGO-CdSe nanorod composite via a facile one-pot solvothermal method and establishes it as an efficient visible-light-driven photocatalyst for norfloxacin degradation. The intimate interfacial coupling between CdSe nanorods and RGO sheets facilitates rapid charge transfer and suppresses electron–hole recombination, resulting in 80.4% degradation within 40 min, which is nearly threefold higher than controlled-CdSe, following pseudo-first-order kinetics with a rate constant of 0.057 min^{-1}. The optimized composite exhibits a 2.35-fold enhancement in apparent quantum yield (0.054%) and a 3.92-fold reduction in electrical energy per order (16.9 kWh m^{-3}), highlighting its improved photon utilization and energy efficiency. Radical scavenging experiments identify photogenerated holes as the dominant oxidative species, supported by hydroxyl and superoxide radicals. The composite retains 90% of its activity after five cycles, and post-reaction XRD analysis confirms its structural and phase stability. Future investigations will focus on evaluating the performance and long-term stability of the RGO-CdSe nanocomposite in diverse water environments, including real wastewater matrices containing competing ions and natural organic matter, to further validate its practical applicability. Overall, this work establishes RGO-CdSe nanorods as a promising hybrid semiconductor nanocomposite platform for energy-efficient solar-driven remediation of antibiotic contaminants in water.

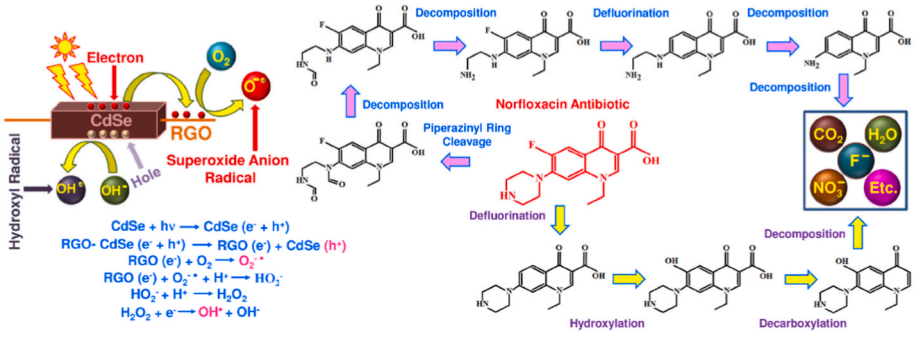

Fig. 7. Mechanistic illustration of norfloxacin photocatalytic degradation by RGO–CdSe, showing reactive species generation and the proposed degradation pathway.

CRediT authorship contribution statement

Subrata Mondal: Writing – original draft, Methodology, Investigation, Formal analysis, Data curation. **Suvendu Ghosh:** Writing – original draft, Methodology, Investigation, Formal analysis, Data curation. **Tanusri Pal:** Writing – review & editing, Project administration, Investigation, Funding acquisition. **Surajit Ghosh:** Writing – review & editing, Supervision, Project administration, Conceptualization.

Declaration of competing interest

The authors declare that they have no known competing financial interests or personal relationships that could have appeared to influence the work reported in this paper.

Acknowledgments

This work was supported by the Department of Science and Technology and Biotechnology (DSTBT), West Bengal, India, through grant no. 625(Sanc)/STBT-11012(26)/2/2024-ST SEC. The authors also acknowledge the Department of Science and Technology (DST) and the University Grants Commission (UGC), New Delhi, India, for providing infrastructural support and special assistance to the Department of Physics, Vidyasagar University, under the FIST and SAP programs, respectively. The first author (SM) is thankful to Department of Social Justice and Empowerment, India, for awarding the Junior Research Fellowship under the scheme of NFSC (Ref No. 221610003767). The authors also thank University Science Instrumentation Centre (USIC), Vidyasagar University, for providing access to the PL facility.

Appendix A. Supplementary data

Supplementary data to this article can be found online at https://doi.org/10.1016/j.ceramint.2026.03.412.

References

[1] D.G.J. Larsson, C.-F. Flach, Antibiotic resistance in the environment, Nat. Rev. Microbiol. 20 (2022) 257–269, https://doi.org/10.1038/s41579-021-00649-x.
[2] R. Laxminarayan, A. Duse, C. Wattal, A.K.M. Zaidi, H.F.L. Wertheim, N. Sumpradit, E. Vlieghe, G.L. Hara, I.M. Gould, H. Goossens, C. Greko, A.D. So, M. Bigdeli, G. Tomson, W. Woodhouse, E. Ombaka, A.Q. Peralta, F.N. Qamar, F. Mir, S. Kariuki, Z.A. Bhutta, A. Coates, R. Bergstrom, G.D. Wright, E.D. Brown, O. Cars, Antibiotic resistance-the need for global solutions, Lancet Infect. Dis. 13 (2013) 1057–1098, https://doi.org/10.1016/S1473-3099(13)70318-9.
[3] H.E. Macedo, B. Lehner, J.A. Nicell, U. Khan, E.Y. Klein, Antibiotics in the global river system arising from human consumption, PNAS Nexus 4 (2025), https://doi.org/10.1093/pnasnexus/pgaf096.
[4] T.U. Berendonk, C.M. Manaia, C. Merlin, D. Fatta-Kassinos, E. Cytryn, F. Walsh, H. Bürgmann, H. Sørum, M. Norström, M.-N. Pons, N. Kreuzinger, P. Huovinen, S. Stefani, T. Schwartz, V. Kisand, F. Baquero, J.L. Martinez, Tackling antibiotic resistance: the environmental framework, Nat. Rev. Microbiol. 13 (2015) 310–317, https://doi.org/10.1038/nrmicro3439.
[5] F. Sun, W. Wang, C. Luo, Z. Song, D. Li, T. Wang, Y. Yang, Q. Ma, W. Yu, X. Dong, Tri-functional $La_2Ti_2O_7$ nanofibers decorated with CdS nanoparticles heterojunction photocatalysts for efficient hydrogen generation, degradation of organic dye and antibiotic, Ceram. Int. 51 (2025) 56173–56184, https://doi.org/10.1016/j.ceramint.2025.09.332.
[6] B. Qin, J. Chen, F. Xu, J. Zou, W. Wang, Y. Lv, L. Tian, L. Zhou, J. Feng, ZIF-8 derived ZnS/ZnO type-II heterojunction for efficient photocatalytic hydrogen peroxide production and norfloxacin degradation, J. Alloys Compd. 1038 (2025) 182866, https://doi.org/10.1016/j.jallcom.2025.182866.
[7] M. Zheng, Y. Li, F. Ma, M. Liang, X. Zhang, J. Wang, J. Zhao, W. Li, Y. Shao, X. Wu, Mesoporous graphitic carbon nitride nanostructure-based antibiotic degradation via synergistic adsorption and photocatalysis: a review, ACS Appl. Nano Mater. 9 (2026) 4053–4080, https://doi.org/10.1021/acsanm.5c04533.
[8] L. Zhang, J. Zhang, J. Yu, H. García, Charge-transfer dynamics in S-scheme photocatalyst, Nat. Rev. Chem 9 (2025) 328–342, https://doi.org/10.1038/s41570-025-00698-3.
[9] L.V. Samarasinghe, S. Muthukumaran, K. Baskaran, Heterojunction photocatalysts for solar-driven wastewater treatment: interfacial design, charge carrier dynamics, and advanced characterization techniques, J. Water Process Eng. 79 (2025) 108960, https://doi.org/10.1016/j.jwpe.2025.108960.
[10] X. Wang, Z.-Y. Yuan, Insights into semiconductor heterojunctions for enhanced photocatalytic performance and applications, Coord. Chem. Rev. 548 (2026) 217184, https://doi.org/10.1016/j.ccr.2025.217184.
[11] A. Balapure, J. Ray Dutta, R. Ganesan, Recent advances in semiconductor heterojunctions: a detailed review of the fundamentals of photocatalysis, charge transfer mechanism and materials, RSC Appl. Interfaces 1 (2024) 43, https://doi.org/10.1039/D3LF00126A.
[12] Q. Liu, S. Ji, Z. Zhao, Y. Hu, Y. Zhang, L. Shi, The enhanced and stable photocatalytic performance over organic–inorganic perylene diimide-$Mn_xCd_{1x}S$ photocatalyst, Appl. Surf. Sci. 724 (2026) 165701, https://doi.org/10.1016/j.apsusc.2025.165701.
[13] S. Kar, T. Pal, S. Ghosh, Reduced graphene oxide - SnSe nanocomposite photocatalyst with high apparent quantum yield for the photodegradation of norfloxacin, ACS Appl. Nano Mater. 7 (2024) 6516–6524, https://doi.org/10.1021/acsanm.4c00282.
[14] A.K. Ranade, A. Yamaguchi, M. Miyauchi, S. Ramaswami, C. Yoshimura, Interface dependent electron shunting in graphene-integrated intimately coupled photocatalytic biodegradation, Water Res. 273 (2025) 123064, https://doi.org/10.1016/j.watres.2024.123064.
[15] D.R. Rout, H.M. Jena, A. Kumar, O. Baigenzhenov, A. Hosseini-Bandegharaei, Graphene-, GO-, and rGO-supported photocatalysts for degradation of organic pollutants: a comprehensive review, Environ. Technol. Innov. 40 (2025) 104560, https://doi.org/10.1016/j.eti.2025.104560.
[16] A.R. Patel, A.D. Fazal, T.D. Solanky, S. Dhibar, S. Kumar, S.K. Panja, Recent advances and challenges in graphene-based nanomaterials for photocatalytic CO_2 reduction, Mater. Adv. 7 (2026) 109–143, https://doi.org/10.1039/D5MA00750J.
[17] A. Mondal, A. Prabhakaran, S. Gupta, V.R. Subramanian, Boosting photocatalytic activity using reduced graphene oxide (RGO)/semiconductor nanocomposites: issues and future scope, ACS Omega 6 (2021) 8734–8743, https://doi.org/10.1021/acsomega.0c06045.
[18] A. Ali, M. Shoeb, B. Li, M.A. Khan, Photocatalytic degradation of antibiotic drug and dye pollutants under visible-light irradiation by reduced graphene oxide decorated MoO_3/TiO_2 nanocomposite, Mater. Sci. Semicond. Process. 150 (2022) 106974, https://doi.org/10.1016/j.mssp.2022.106974.
[19] D.S. Vavilapalli, L. Qin, J. Palisaitis, J. Rosen, Enhanced photocatalytic performance of a rGO-$Ca_2Fe_2O_5$ nanocomposite for photodegradation of emergent pollutants, npj Clean Water 7 (2024) 41, https://doi.org/10.1038/s41545-024-00334-5.
[20] A.T. Ahmed, F.M.A. Altalbawy, H.R.A.K. Al-Hetty, N. Fayzullaev, J.K. V, J. Sharma, F. F, B. Abd, A.M. Ahmed, H. Noorizadeh, Cadmium selenide quantum dots in photo- and electrocatalysis: advances in hydrogen, oxygen, and CO_2 reactions, Mater. Sci. Semicond. Process. 199 (2025) 109831, https://doi.org/10.1016/j.mssp.2025.109831.
[21] G. Ramalingam, C.M. Magdalane, B.A. Kumar, R. Yuvakkumar, G. Ravi, A.I. Jothi, N.K. Rotte, G. Murugadoss, A. Ananth, Enhanced visible light-driven photocatalytic performance of CdSe nanorods, Environ. Res. 203 (2022) 111855, https://doi.org/10.1016/j.envres.2021.111855.
[22] D. Khandelwal, D. Jain, P.R. Solanki, K.R. Ranjan, M. Das Mukherjee, A novel nanocomposite platform of mercaptopropionic acid stabilized CdSe quantum dots-graphene for impedimetric detection of low density lipoprotein, Mater. Lett. 308 (2022) 131236, https://doi.org/10.1016/j.matlet.2021.131236.
[23] I.A. Mkhalid, A. Shawky, Visible light-active CdSe/rGO heterojunction photocatalyst for improved oxidative desulfurization of thiophene, Ceram. Int. 46 (2020) 20769–20776, https://doi.org/10.1016/j.ceramint.2020.05.033.
[24] A.I. Abdel-Salam, M.M. Awad, T.S. Soliman, A. Khalid, The effect of graphene on structure and optical properties of CdSe nanoparticles for optoelectronic application, J. Alloys Compd. 898 (2022) 162946, https://doi.org/10.1016/j.jallcom.2021.162946.
[25] K. Tsai, Y.-J. Hsu, Graphene quantum dots mediated charge transfer of CdSe nanocrystals for enhancing photoelectrochemical hydrogen production, Appl. Catal. B Environ. 164 (2015) 271–278, https://doi.org/10.1016/j.apcatb.2014.09.034.
[26] D. Patidar, A. Yadav, D.R. Paul, A. Sharma, S.P. Nehra, Nanohybrids cadmium selenide-reduced graphene oxide for improving photo-degradation of methylene blue, Physica E Low Dimens. Syst. Nanostruct. 114 (2019) 113560, https://doi.org/10.1016/j.physe.2019.113560.
[27] E. Tavakolian, J. Tashkhourian, Sonication-assisted preparation of a nanocomposite consisting of reduced graphene oxide and CdSe quantum dots, and its application to simultaneous voltammetric determination of ascorbic acid, dopamine and uric acid, Mikrochim. Acta 185 (2018) 456, https://doi.org/10.1007/s00604-018-2988-y.
[28] K. Chakraborty, P. Das, S. Chakrabarty, T. Pal, S. Ghosh, AC conduction and time – temperature superposition scaling in a reduced graphene oxide – zinc sulfide nanocomposite, ChemPhysChem 17 (2016) 1518–1523, https://doi.org/10.1002/cphc.201501112.
[29] L.F. Xi, Y.M. Lam, Synthesis and characterization of CdSe nanorods using a novel microemulsion method at moderate temperature, J. Colloid Interface Sci. 316 (2007) 771–778, https://doi.org/10.1016/j.jcis.2007.07.067.
[30] G. Wang, Y. Ma, Z. Wei, M. Qi, Development of multifunctional cobalt ferrite/graphene oxide nanocomposites for magnetic resonance imaging and controlled drug delivery, Chem. Eng. J. 289 (2016) 150–160, https://doi.org/10.1016/j.cej.2015.12.072.
[31] K. Chakraborty, T. Pal, S. Ghosh, RGO-ZnTe: a graphene based composite for tetracycline degradation and their synergistic effect, ACS Appl. Nano Mater. 1 (2018) 3137–3144, https://doi.org/10.1021/acsanm.8b00295.

[32] L. Desmurs, A. Galarneau, C. Cammarano, V. Hulea, C. Vaulot, H. Nouali, B. Lebeau, T.J. Daou, C.V. Soares, G. Maurin, M. Haranczyk, I. Batonneau-Gener, A. Sachse, Determination of microporous and mesoporous surface areas and volumes of mesoporous zeolites by corrected *t*-plot analysis, ChemNanoMat 8 (2022) e202200051, https://doi.org/10.1002/cnma.202200051.

[33] A.K. Ladavos, A.P. Katsoulidis, A. Iosifidis, K.S. Triantafyllidis, T.J. Pinnavaia, P. J. Pomonis, The BET equation, the inflection points of N_2 adsorption isotherms and the estimation of specific surface area of porous solids, Microporous Mesoporous Mater. 151 (2012) 126–133, https://doi.org/10.1016/j.micromeso.2011.11.005.

[34] B. Antil, R. Ranjan, C.S. Gopinath, S. Deka, Directed holey and ordered g-$C_3N_{4.5}$ nanosheets by a hard template nanocasting approach for sustainable visible-light hydrogen evolution with prominent quantum efficiency, J. Mater. Chem. A 8 (2020) 13328–13339, https://doi.org/10.1039/D0TA02734K.

[35] T.-B. Nguyen, K. Sherpa, C.-W. Chen, L. Chen, P.N.T. Ho, C.-D. Dong, Enhancing photocatalytic reduction of Cr(VI) in water through morphological manipulation of g-C_3N_4 photocatalysts: a comparative study of 1D, 2D, and 3D structures, Chemosphere 362 (2024) 142787, https://doi.org/10.1016/j.chemosphere.2024.142787.

[36] A.K. Singh, A.N. Yadav, A. Srivastava, K.K. Haldar, M. Tomar, A.V. Alaferdov, S. A. Moshkalev, V. Gupta, K. Singh, CdSe/V_2O_5 core/shell quantum dots decorated reduced graphene oxide nanocomposite for high-performance electromagnetic interference shielding application, Nanotechnology 30 (2019) 505704, https://doi.org/10.1088/1361-6528/ab4290.

[37] Y. Lao, Z. Zhao, Y. Hu, Y. Zhang, L. Shi, Enhanced photocatalytic H_2 evolution performance of a novel Co_3O_4/$ZnIn_2S_4$ composite photocatalyst, Sol. Energy 307 (2026) 114336, https://doi.org/10.1016/j.solener.2026.114336.

[38] Z. Ghaffarbejouei, M. Moosavifar, A. Alemi, Synthesis and investigation of physicochemical behavior and catalytic activity of Sm and Zn-doped CeO_2 nanoparticles, Ceram. Int. 52 (2026) 1891–1903, https://doi.org/10.1016/j.ceramint.2025.12.008.

[39] M.W. Marashdeh, M.I. Sayyed, K.A. Mahmoud, K.J. Sandougah, S. Biradar, The influence of substitution of Te^{4+} and Sm^{3+} for B^{3+} ions on the optical, mechanical, and radiation shielding properties of boro-tellurite glasses, Ceram. Int. 52 (2026) 4527–4539, https://doi.org/10.1016/j.ceramint.2025.12.226.

[40] P.V. Do, L.D. Thanh, T.T.C. Thuy, N.V. Nghia, N.M. Hung, N.T.M. Thuy, N.T. Hien, N.X. Ca, An in-depth study of the structure, optical properties and energy transfer process of Eu^{3+}-doped CdSe nanocrystals, Ceram. Int. 51 (2025) 6616–6626, https://doi.org/10.1016/j.ceramint.2024.12.106.

[41] K. Chakraborty, S. Ghosh, T. Pal, Reduced-graphene-oxide zinc-telluride composite: towards large-area optoelectronic and photocatalytic applications, ChemistrySelect 3 (2018) 8637–8643, https://doi.org/10.1002/slct.201801519.

[42] X. Wang, S. Ji, Y. Zhang, L. Shi, High-efficiency photocatalytic H_2-evolution in water/seawater over a novel noble metal free Ni_3C/$Mn_{0.5}Cd_{0.5}S$ Schottky junction, J. Colloid Interface Sci. 678 (2025) 1043–1051, https://doi.org/10.1016/j.jcis.2024.08.219.

[43] R.J. Baxter, P. Hu, Insight into why the Langmuir-Hinshelwood mechanism is generally preferred, J. Chem. Phys. 116 (2002) 4379–4381, https://doi.org/10.1063/1.1458938.

[44] S. Shin, T.H. Seo, J. Lee, Growth kinetics of carbon nanotubes in a fluidized bed reactor: a Langmuir-Hinshelwood approach, Ind. Eng. Chem. Res. 64 (2025) 14802–14812, https://doi.org/10.1021/acs.iecr.5c01140.

[45] H.D. Tran, D.Q. Nguyen, P.T. Do, U.N.P. Tran, Kinetics of photocatalytic degradation of organic compounds: a mini-review and new approach, RSC Adv. 13 (2023) 16915–16925, https://doi.org/10.1039/D3RA01970E.

[46] S. Kar, S. Ghosh, T. Pal, MoS_2-CdS composite for photocatalytic reduction of hexavalent chromium and thin film optoelectronic device applications, Sci. Rep. 14 (2024) 18674, https://doi.org/10.1038/s41598-024-69530-0.

[47] S. Ghosh, S. Kar, T. Pal, S. Ghosh, MoS_2-CdS composite photocatalyst for enhanced degradation of norfloxacin antibiotic with improved apparent quantum yield and energy consumption, J. Phys. Chem. Solid. 193 (2024) 112144, https://doi.org/10.1016/j.jpcs.2024.112144.

[48] R. Nag, D. Das, S. Manna, S. Sasmal, A. Thander, A. Bera, Ti_3C_2 MXene modified porous $NiTiO_3$ nanorod Schottky heterojunction towards enhanced photocatalytic dye degradation, Mater. Today Commun. 37 (2023) 107330, https://doi.org/10.1016/j.mtcomm.2023.107330.

[49] D. Dai, L. Wang, N. Xiao, S. Li, H. Xu, S. Liu, B. Xu, D. Lv, Y. Gao, W. Song, L. Ge, J. Liu, In-situ synthesis of Ni_2P co-catalyst decorated $Zn_{0.5}Cd_{0.5}S$ nanorods for high-quantum-yield photocatalytic hydrogen production under visible light irradiation, Appl. Catal., B 233 (2018) 194–201, https://doi.org/10.1016/j.apcatb.2018.04.013.

[50] R. Nag, S. Manna, D. Das, A. Jana, A. Bera, A spin-polarized electron-induced MXene-$KBi_{0.9}Co_{0.1}Fe_2O_5$ photocatalyst for enhanced dye degradation, Adv. Eng. Mater. 26 (2024) 2401478, https://doi.org/10.1002/adem.202401478.

[51] N.A. Waghchoure, A. Patel, L.G. Raikar, J. Gandhi, K.P. Jayadevan, H. Prakash, Removal of tetracycline antibiotic activity in water by stable cubic phase barium stannate-perovskite nanoparticles under energy-efficient blue light LED irradiation, RSC Adv. 15 (2025) 22250–22266, https://doi.org/10.1039/d5ra02938d.

[52] R. Nawaz, M.M. Hanafiah, Z. Sakawi, Z.A. Baki, S.B.Z. Abidin, M. Anjum, A. F. Ismail, U. Arshad, A review of the defective TiO_2 materials-based photocatalysis for environmental remediation: exploring the nexus between light wavelength and energy consumption, Appl. Energy 393 (2025) 126143, https://doi.org/10.1016/j.apenergy.2025.126143.

[53] A.E. Khyave, R. Mafigholmi, A. Davood, A. Mahvi, L. Salimi, Photocatalytic degradation of azithromycin and ceftriaxone using synthesized Ag/g-C_3N_4/Fe_3O_4 nanocomposites in aqueous solution, Sci. Rep. 15 (2025) 18726, https://doi.org/10.1038/s41598-025-00149-5.

[54] J. Zhang, X. Wang, Y. Zhang, R. Li, Z. Xing, M. Lu, Degradation of norfloxacin by magnetic recyclable Z-scheme heterojunctions $CoWO_4$/$ZnFe_2O_4$ photocatalysts, J. Alloys Compd. 1014 (2025) 178740, https://doi.org/10.1016/j.jallcom.2025.178740.

[55] H. Lin, W.H. Hassan, H.A. Abbood, S. Samad, C. Yang, M.A. Diab, H.A. El-Sabban, D. Jumanazarov, F. Atamurotov, B. Samandarov, P. Zhu, Designing a novel Ti_3C_2 MXene-bridged Z-scheme photocatalyst for effective H_2 generation and removal of non-biodegradable norfloxacin: optimization and mechanism insights, J. Alloys Compd. 1031 (2025) 181029, https://doi.org/10.1016/j.jallcom.2025.181029.

[56] H. Yang, J. Li, Q. Su, B. Wang, Z. Zhang, Y. Dai, Y. Li, L. Hou, Construction of Bi_2MoO_6/$CoWO_4$ Z-scheme heterojunction for high-efficiency photocatalytic degradation of norfloxacin under visible light: performance and mechanism insights, Chem. Eng. J. 470 (2023) 144139, https://doi.org/10.1016/j.cej.2023.144139.

[57] J. Song, M. Li, M. Song, P. Liu, X. Lin, N. Xing, Y. Wu, L. Li, Dual in-situ construction of CAU-17-derived Bi/BiOBr/$Bi_4O_5Br_2$ S-scheme heterojunction: enabling efficient degradation of norfloxacin, J. Alloys Compd. 1040 (2025) 183710, https://doi.org/10.1016/j.jallcom.2025.183710.

[58] U. Mahajan, A. Srivastava, A. Kumar, M. Dhonde, K. Sahu, P.M. Shirage, Cr-doped barium stannate perovskite as an advanced photocatalyst for degrading carcinogenic rhodamine B, Ceram. Int. 52 (2026) 1083–1095, https://doi.org/10.1016/j.ceramint.2025.11.412.

[59] S.C. Shyagathur, A. Hiremath, J. Pattar, R. Sreekanth, K. Mahendra, H.N. Anil Rao, Visible light harvesting using ZnS/rGO/g-C_3N_4 heterojunction for crystal violet dye degradation: kinetic and mechanistic insights, Ceram. Int. 52 (2026) 1818–1830, https://doi.org/10.1016/j.ceramint.2025.11.445.

[60] D. Dwiyanti, M. Irsan, D.S. Mulus, Y. Deawati, S. Solihudin, T. Takei, D.R. Eddy, M. D. Permana, Enhanced photocatalytic activity by structural defect of ZnO/SiO_2 composite for removal of methylene blue, Ceram. Int. 51 (2025) 45419–45430, https://doi.org/10.1016/j.ceramint.2025.07.258.

[61] S. Ghosh, S. Nandi, S. De, T. Pal, S. Ghosh, Solution-processed $CdS_{1-x}Se_x$ nanorods with composition-tuned bandgap and microstructural evolution for visible-light photocatalytic response, J. Phys. Chem. Solid. 212 (2026) 113565, https://doi.org/10.1016/j.jpcs.2026.113565.

[62] C. Zhang, M. Jia, Z. Xu, W. Xiong, Z. Yang, J. Cao, H. Peng, H. Xu, Y. Xiang, Y. Jing, Constructing 2D/2D N-ZnO/g-C_3N_4 S-scheme heterojunction: efficient photocatalytic performance for norfloxacin degradation, Chem. Eng. J. 430 (2022) 132652, https://doi.org/10.1016/j.cej.2021.132652.